Short Report

Magnetized Biochar as a Gold Nanocatalyst Support for *p*-Nitrophenol Reduction

Renata P. Lopes, ✱,a,b Tiago Guimarães[a] and Didier Astruc ✱,b

aDepartamento de Química, Universidade Federal de Viçosa, 36570-900 Viçosa-MG, Brazil

bUniversité de Bordeaux, ISM, UMR CNRS 5255, Talence 33405 Cedex, France

The biomass use is of considerable ecological and economical interest and here, biochar, a by-product of biomass carbonization, is magnetized with Fe_3O_4 for its use as gold nanoparticle (NP) support towards catalysis of *p*-nitrophenol (4-NP) reduction. Biochar was synthesized from coffee straw biomass via pyrolysis, while magnetite functionalization was obtained using the precipitation method. The magnetite was identified by X-ray diffraction (XRD). The material had a specific surface area of 30 m^2 g^{-1} and a zero point charge of 7.5. The gold NPs were deposited via reduction with $NaBH_4$, which yielded Au and Fe_3O_4 NP of 4.61 and 10.9 nm, respectively. The materials were applied in the 4-NP reduction, with a rate constant $k_{app} = (1.2 \pm 0.2) \times 10^{-2}$ s^{-1}, and a synergistic effect between Au and Fe_3O_4 NPs was observed. Remarkably, comparison with graphene oxide to which biochar resembles showed similar behavior, and the material was reused in several catalytic cycles.

Keywords: biochar, magnetic support, gold nanoparticles, nanocatalysis nitrophenol reduction

Introduction

Gold nanoparticles (AuNPs)[1] are known as excellent catalysts for many redox reactions including oxidation by CO and alcohols by oxygen, epoxidation of propylene, and hydrogenation of multiple carbon-carbon bonds.[1-8] The AuNP size[2,9,10] and support nature[3,7,8] have been shown to play a key role in AuNP stabilization and catalytic efficiency and selectivity. Besides oxides, first popularized by Haruta and Daté[2] upon synthesis of small AuNPs, active carbons, diamonds, phosphates, among others are current AuNP supports. Engineered support nanostructures have been designed including nanoporous materials (zeolites, mesoporous silica, metal organic frameworks), magnetic materials (iron oxides), and yolk-shell or core-shell nanostructures.[7,8]

Biomass utilization in the context of AuNP catalysis is of fundamental and ecological interest, and biochar is a by-product obtained by biomass carbonization that might be suitable for this application. Biochar (BC) contains stacks of graphite agglomerates with graphene layers and a graphene oxide (GO)-type structure whose edge carbons are potential sites for catalytic synergies with AuNPs. There is thus great interest in the use of biochar as support in catalysis as shown by a growing literature.[11-15] Jiang and co-workers[16] reported that the addition of magnetite nanoparticles to biochar significantly improved the efficiency of the catalysts, in addition to adding magnetic properties to the material, enabling its easy recovery from the reaction medium and facilitating its reuse.

One of the most common reactions used as a probe to study the activity of new catalysts is the reduction of *p*-nitrophenol (4-NP).[17] 4-NP is known to be a by-product from pesticides, herbicides and synthetic dyes, which can cause damage to the central nervous system, liver, kidney, and both animal and human blood.[18] This reaction is a "model catalytic reaction" due to the advantages of producing only one product from a simple reagent at mild temperatures and the reaction in the absence of catalyst is very slow.[19] Significantly, the reaction can be easily monitored by UV-Vis spectroscopy monitoring the absorption decrease of 4-nitrophenolate ions at 400 nm.[20] Au and Pd[17] nanoparticles (NPs) have the most successful nanocatalysts for this reaction.[21]

The goal of this work was to synthesize AuNPs supported on biochar functionalized with magnetite ($Au@BC-Fe_3O_4$) and to apply such a BC-based nanocomposite as efficient and recyclable nanocatalyst of *p*-nitrophenol (4-NP) reduction by $NaBH_4$[18-20,22,23] using this cheap ecological biomass-valued support.

*e-mail: renata.plopes@ufv.br; didier.astruc@u-bordeaux.fr

Experimental

Chemicals and reagents

Sodium hydroxide (CAS 1310-73-2) was obtained from Fisher (Waltham, USA), and *p*-nitrophenol (CAS 100-02-7) was obtained from Acros Organics (Geel, Belgium). Sodium borohydride (CAS 16940-66-2) and trihydrate chloroauric acid (CAS 16961-25-4) were obtained from Alfa Aesar (Haverhill, USA). Iron sulfate heptahydrate (CAS 7782-63-0) was obtained from Sigma-Aldrich (St. Louis, USA). Hydrochloric acid 37% (CAS 7647-01-0) was purchased from Quemis (Joinville, Brazil). Aqueous solutions were prepared with water type 1 obtained by Milli-Q system (Millipore Corp., Bedford, MA, USA).

Biochar preparation

Arabica coffee straw (*Coffea arabica*) was collected in Espírito Santo-Brazil, latitude: 20°45'49"S, longitude: 41°31'59"W. The straw was subjected to a washing step with distilled water and dried to 80 °C for 48 h. The dry material was ground in a knife mill, and the resulting biomass was then subjected to a pyrolysis stage at 600 °C in an oxygen-free atmosphere, with a residence time of 4 h. The biochar produced was sieved, which provided 20 to 200 mesh particles.

Synthesis of the materials

The BC (2.0 g) was added to NaOH (20 mL, 0.2 mol L^{-1}) and FeSO$_4$·7H$_2$O (2 mL, 1 mol L^{-1}). The system was agitated (1 h, 100 °C), centrifugated, and the supernatant was removed. The solid was washed with water and dried at 60 °C (BC-Fe$_3$O$_4$). BC was obtained under the same conditions, except for FeSO$_4$ addition.

HAuCl$_4$·3H$_2$O (0.275 mmol in 10 mL ethanol) was transferred to 0.5 g BC (BC or BC-Fe$_3$O$_4$) and stirred for 3 h. The solvent was evaporated, NaBH$_4$ (10 mL, 0.25 mol L^{-1}) was added, and the system was stirred (30 min). After centrifugation, the supernatant was removed. The solid was dried at 60 °C (Au@BC and Au@BC-Fe$_3$O$_4$). GO was synthesized using the Hummers method.[24] Au@GO and Au@GO-Fe$_3$O$_4$ were synthesized as described above, except for BC use.

Characterization

Fourier transform infrared (FTIR) spectroscopy

The materials were analyzed by Bruker VERTEX 70 instrument (Billerica, USA) using the attenuated total reflection (ATR) method in the range of 350-4000 cm^{-1}.

Raman spectroscopy

The materials were analyzed by micro-Raman Renishaw InVia spectrometer (Gloucestershire, England) equipped with an Nd-YAG laser (λ_0 = 514 nm) and a 50× objective lens (Olympus B×41). The acquisition time of Raman spectrum for each sample was set as 10 s.

X-ray diffraction (XRD) analyses

The materials were analyzed a D8-Discover BRUKER equipment (Massachusetts, USA), equipped with a copper tube (1.5418 Å), sweeping the range from 10 to 80° 2θ with a 0.05° step.

Point of zero charge (PZC)

The procedure used was adapted from Wang *et al.*[25] 20 mg of material was added in 25 mL of NaCl solution (0.100 mol L^{-1}), under 11 different initial pH (2, 3, 4, 5, 6, 8, 9, 10, 11, 12,13), adjusted by HCl or NaOH solutions (both at 0.100 mol L^{-1}). The system was stirred at 100 rpm and at 25 °C during 24 h. After this, the solutions were filtered, and the final pH was analyzed. The PCZ corresponds to the range in which the final pH remains constant regardless of the initial pH; that is, the surface acts as a buffer. The assays were performed in triplicate.

Transmission electron microscopy (TEM)

The materials were analyzed by TEM using a JEOL JEM 1400 (120 kV) microscope (Tokyo, Japan).

Surface morphology and elemental analysis of biochar were carried out by scanning electron microscopy (SEM) coupled with X-ray energy dispersive spectrometry (EDS), in a scanning electron microscope, brand JEOL, model JSM-6010LA (Tokyo, Japan). This microscope has a resolution of 4 nm (with beam at 20 kV), magnification from 8× to 300,000× and acceleration voltage from 500 V to 20 kV. Electron gun was utilized with a pre-centered tungsten filament. An Everhart-Thornley detector provided secondary electron images and solid state detector was used for retro-scattered electrons with contrast of topography, composition and variable shading. A silicon drift detector served for EDS analysis with 133 eV resolution.

4-NP reduction

0.15 mL of a 4-NP (0.80 mmol L^{-1}), 0.15 mL of NaBH$_4$ (80 mmol L^{-1}), 2.70 mL of water type 1 were added into a cuvette (1 cm optical path). Then, 30 µL of a material suspension (5 mg mL^{-1}) were added in the system, and the

time started to be monitored. The system was maintained at room temperature (ca. 25 °C) and the reaction was monitored for 10 min by UV-Vis spectroscopy (Cary 100 Scan, Addison, USA) in full scan mode (250-500 nm). The experiments were carried out in duplicate.

Results and Discussion

Different techniques were utilized to characterize the formation of the biochar materials obtained from the carbonization of biomass and magnetite using the chemical precipitation method. First, the BC before and after magnetite and Au NPs deposition functionalization was analyzed by FTIR, and the results are shown in Figure 1. There were no significant changes after functionalization, with bands at 3352 cm^{-1} assigned to the stretching of O–H bond, 1632 cm^{-1} assigned to the stretching vibration of carbonyl/carboxyl (C=O) bond, 1348 cm^{-1} assigned to the vibration of C=C bond, and 1030 cm^{-1} assigned to the vibration of C–O bonds.[15] These bands are characteristic of BC from different biomass, such as swine bone,[26] pine needles of *Pinus koraiensis*[27] and sewage sludge.[28] The magnetic property was also shown by approaching a magnet to the material.
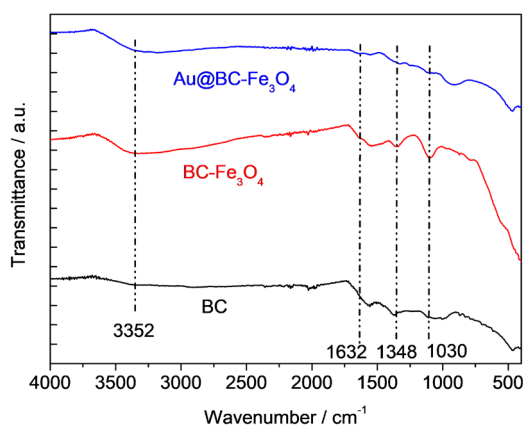

Figure 1. FTIR spectra of BC, BC-Fe$_3$O$_4$ and Au@BC-Fe$_3$O$_4$.

Another important characterization technique is Raman spectroscopy, for which the results are described in Figure 2. Bands were identified at 1359 cm^{-1}, assigned to the D band referring to graphite, due to the breathing mode of A$_{1g}$ symmetry[15] and at 1580 cm^{-1}, assigned to the G band referring to amorphous carbon representing the in-plane bond-stretching motion of pairs of sp^2 carbon atoms in chains and rings demonstrating the existence of graphitic carbon.[15] These bands are characteristic of BC and have been described by different authors.[26,28] The degree of carbon material disorder, obtained by the ratio between the D intensity band and the G intensity band (I$_D$/I$_G$), is 0.81. After BC functionalization with magnetite, a band

was observed at 679 cm^{-1}. According to Gasparov *et al.*,[29] this band can be assigned to the A$_{1g}$ vibration mode that involves the stretching vibrations of the oxygen atoms along the Fe–O bonds.
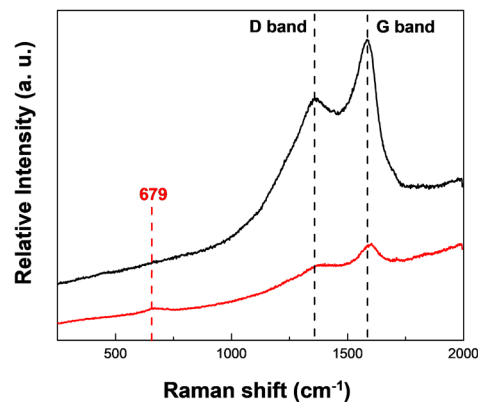

Figure 2. Raman spectra of BC before (—) and after magnetite functionalization (—).

XRD analyses before and after the functionalization with magnetite and Au NPs depositions are shown in Figure 3.
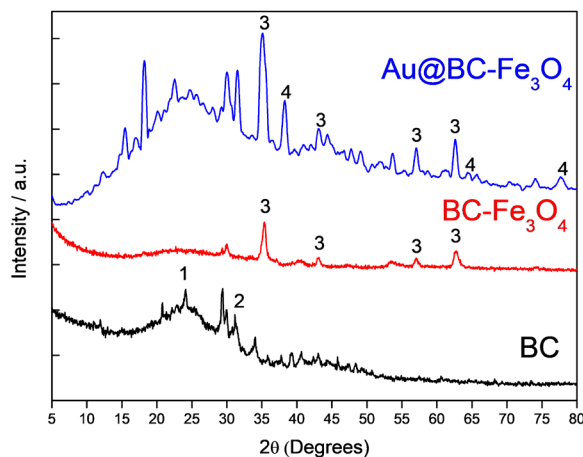

Figure 3. X-ray diffractograms of BC before and after functionalization. 1: amorphous carbon, 2: silica, 3: magnetite and 4: gold.

The BC before magnetite functionalization showed a wide peak at 2θ = 10-30° that represents the (002) diffraction plan of graphite.[15] Similar results were also observed in others works *inter alia* by Wang *et al.*[30] and Jiang *et al.*[16] The presence of silica 2θ = 30° is due to the natural presence of this element in the precursor biomass in the biochar production.[31] After functionalization, characteristic peaks of magnetite can be observed including peaks 2θ and their indexed planes are 35.50° (311), 43.02° (400), 57.03° (511), 62.70° (440).[16] The diffraction peaks at 2θ values of 38.35, 64.6 and 77.7° are attributed to the (111), (220) and (311) diffractions of the fcc structure of gold.[32]

The N_2 adsorption/desorption isotherm for BC-Fe_3O_4 is shown in Figure 4. The specific surface area for BC before and after functionalization was 1.242 and 29.98 m^2 g^{-1}, respectively. Possibly, the increase in the surface area is due to the functionalization step with magnetite, in which a NaOH solution, widely used as a BC activating agent,[15] was used. The presence of NaOH provokes the separation between the lamellae constituted by plane aromatic compound containing layers of graphene/graphite structures and the functional groups at the edges of the lamellae, allowing them to completely crinkle. In the presence of water, the lamellae cannot return to their previous state.[33] Jiang *et al.*[34] synthesized magnetic biochar from $FeCl_3$-preloaded sawdust via pyrolysis as support for Pd NPs whose material presented a specific surface area of 340.6 m^2 g^{-1}. In another work, Jiang and co-workers[16] synthesized Pd@Fe_3O_4/biochar with surface area of 295.4 m^2 g^{-1}. The difference in specific surface area can be attributed to biomass and the carbonization process used. The PZC was 7.5. Karunanayake *et al.*[35] obtained magnetic BC from waste Douglas fir with PZC of 6.25.
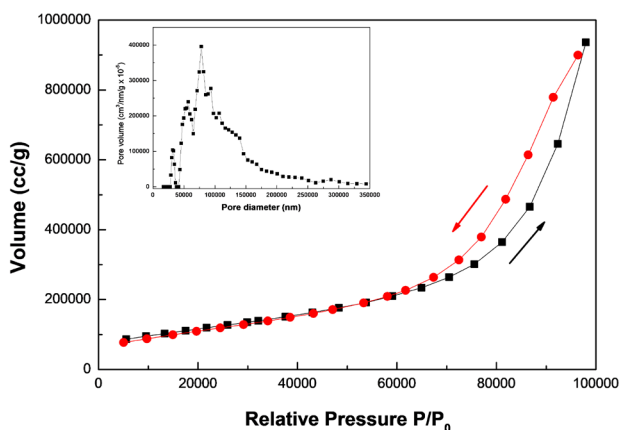
Images obtained by TEM are shown in Figure 5. *Quasi*-spherical NPs with a size of 10.9 ± 2.4 nm are observed in the BC-Fe_3O_4 that can be attributed to magnetite NPs (Figure 5a). Similar results were obtained by Liyanage *et al.*,[36] who obtained Fe_3O_4 particles of 12.3 ± 7.1 nm dispersed on the BC surface. In addition to magnetite, spherical AuNPs are observed with a size of 4.6 ± 1.0 nm (Figure 5b). Carbon-based lamellar structures can be seen in Figure 6a. It is also possible to observe the homogeneous distribution of iron on the carbon structure (Figure 6c). As observed by EDS (Figure 7), the elements present in the composition of Au@BC-Fe_3O_4 are carbon, iron, silicon, potassium, calcium and oxygen. However, carbon and iron are in greater quantity. Gold cannot be observed by this technique, possibly due to its low sensitivity. However, the presence of AuNPs was clearly observed in the XRD (Figure 3).

The 4-NP reduction by different materials are shown in Figure 8 and Table 1. BC-Fe_3O_4 and Au@BC (Figures 8b-8c) presented a similar behavior, with rate constant (k_{app}) of 4.6 × 10^{-3} and 4.7 × 10^{-3} s^{-1}, respectively. Compared to BC (Figure 8d) that has a k_{app} of 9.0 × 10^{-4} s^{-1}, Au@BC and BC-Fe_3O_4 presented a ca. 5-time larger k_{app}. However, Au@BC-Fe_3O_4 showed a significantly higher constant (1.20 × 10^{-2} s^{-1}), with an induction time (t_0) of only 34 s. These results prove a synergistic effect between AuNPs and Fe_3O_4, because the kinetics was significantly higher in comparison to the two materials BC-Fe_3O_4 and Au@BC, as can be seen in Table 1. The reactivity order of the materials was: Au@BC-Fe_3O_4 > Au@BC ca. BC-Fe_3O_4 > BC. The efficiency of BC is compared with GO (Table 1), and the results are very close with both supports showing a similar tendency. Similar results were obtained by Jiang *et al.*,[16] who described the 4-NP reduction by Pd@Fe_3O_4/BC with k_{app} of 2.4 ×10^{-2} s^{-1}. Sahiner *et al.*[37] reported the synthesis of hydrogel based on acrylamide-chicken

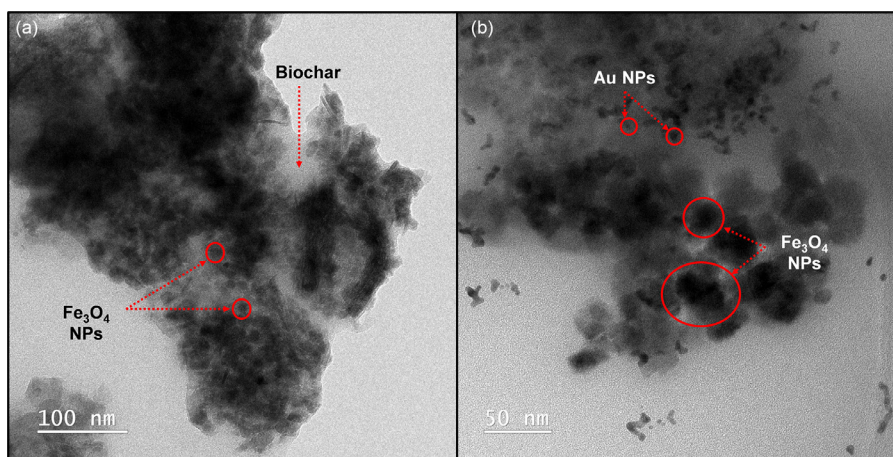**Figure 4.** Nitrogen adsorption-desorption isotherms of BC-Fe_3O_4. Inset: pore distribution of BC-Fe_3O_4.

Figure 5. Transmission electronic microscopy (TEM) (a) BC-Fe_3O_4, (b) Au@BC-Fe_3O_4, Fe_3O_4 size: 10.9 ± 2.4; Au NPs size: 4.61 ± 1.01 nm.
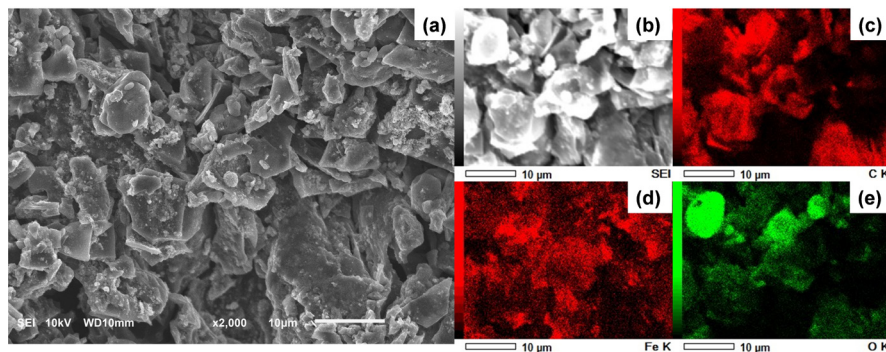
Figure 6. (a) SEM image obtained from Au@BC-Fe$_3$O$_4$. (b) Mapping of chemical elements by EDS, (c) C mapping, (d) Fe mapping, (e) O mapping.
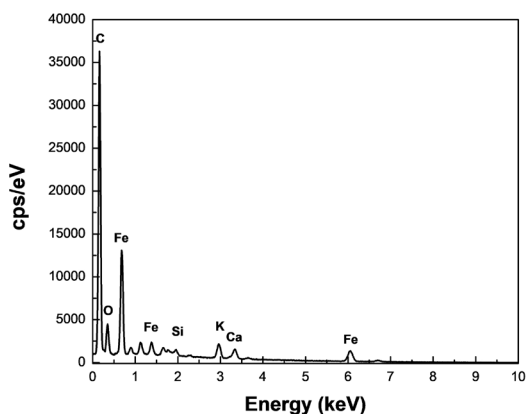

Figure 7. EDS analysis of Au@BC-Fe$_3$O$_4$.

biochar and its use as a template in the preparation of silver metal nanoparticles and applied them to the reduction of *p*-nitrophenol, obtaining a constant kinetics of 6.2×10^{-4} s^{-1} at 30 °C.

Based on these results, it can be proposed that the BH$_4^-$ anion coordinates to the AuNPs surface, transferring electrons to it. The epoxy, carboxyl and phenolic groups of BC allow charge distribution between AuNPs and BC. The electrons at the interface of Au-Fe$_3$O$_4$ are more active due to different surface energy of AuNPs and Fe$_3$O$_4$.[32-34] Meanwhile, the *p*-nitrophenolate anion is attracted to the positive surface of BC by electrostatic interactions. The excess electrons facilitate the capture of electrons by 4-NP,
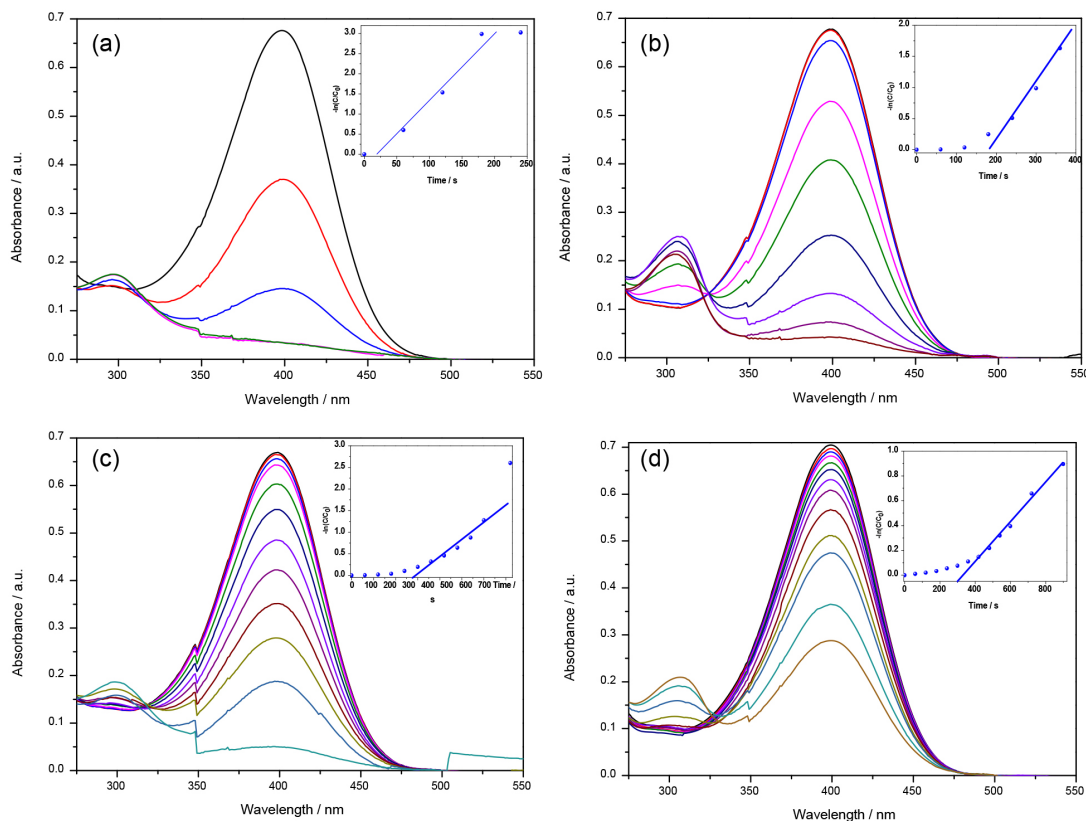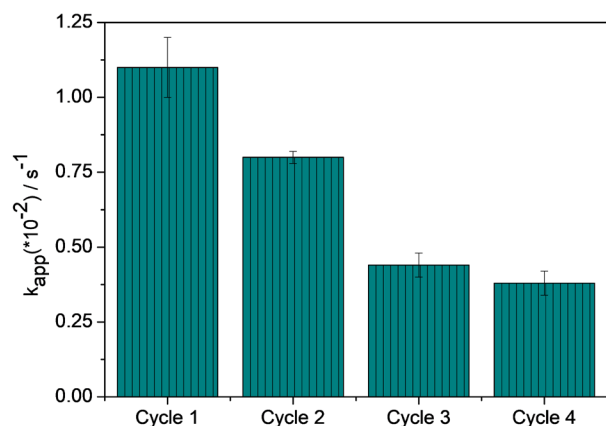

Figure 8. *p*-NP reduction by NaBH$_4$. (a) Au@BC-Fe$_3$O$_4$, (b) BC-Fe$_3$O$_4$, (c) Au@BC and (d) BC. Conditions: 4-NP: NaBH$_4$ (molar ratio 1:100); catalyst: 30 μL of suspension 5 mg mL^{-1}. Inset: *p*-NP reduction by NaBH$_4$ kinetic curve.

Table 1. Induction time (t_0) and decay rate constant (k_{app}) for 4-NP reduction. Conditions:4-NP:NaBH$_4$ (molar ratio 1:100); catalyst: 30 µL of suspension 5 mg mL^{-1}

Material	t_0^a / s	k_{app} / s^{-1}	Material	t_0 / s	k_{app} / s^{-1}
Au@BC-Fe$_3$O$_4$	34	$(1.2 \pm 0.2) \times 10^{-2}$	Au@GO^b-Fe$_3$O$_4$	38	9.78×10^{-1}
BC-Fe$_3$O$_4$	171	$(4.6 \pm 2.9) \times 10^{-3}$	GO^b-Fe$_3$O$_4$	42	7.00×10^{-4}
Au@BC	271	$(4.7 \pm 0.9) \times 10^{-3}$	Au@GO^b	182	6.80×10^{-3}
BC	327	$(9.0 \pm 4.0) \times 10^{-4}$			

^{a}The induction time (t_0) values refer to the inset of Figure 8; ^{b}GO was synthesized using the Hummers method.[24] BC: biochar; GO: graphene oxide.

Figure 9. Reusability of the Au@BC-Fe$_3$O$_4$ catalyst for 4-NP reduction by NaBH$_4$. Conditions: 4-NP:NaBH$_4$ (molar ratio 1:100); catalyst: 30 µL of suspension 5 mg mL^{-1}.

allowing their reduction. The release of *p*-aminophenol creates a free surface, and the catalytic cycle starts again.[34]

The reuse of the catalyst was conducted (Figure 9), and the kinetic constant decreased from 1.1×10^{-2} for 8.0×10^{-3}, 4.4×10^{-3} and 3.8×10^{-3} s^{-1} in the second, third and fourth cycle, respectively. Despite this decrease, improvements remain potentially feasible, for instance upon BC functionalization.

Conclusions

BC has been used here as a support of Au-catalyzed 4-NP reduction. In addition to contributing to the synergy between Fe$_3$O$_4$ and AuNPs whose effect consists of approximately 3-times increase in the 4-NP reduction kinetics, the magnetization allows easy separation of the catalyst, facilitating its reuse. For future research, the functionalization of BC should improve the catalytic efficiency in multiple catalytic cycles, and this system could be applied to other catalytic reactions.

Acknowledgments

References

1. Daniel, M. C.; Astruc, D.; *Chem. Rev.* **2004**, *104*, 293.

2. Haruta, M.; Daté, M.; *Appl. Catal., A* **2001**, *222*, 427.

3. Ishida, T.; Murayama, T.; Taketoshi, A.; Haruta, M.; *Chem. Rev.* **2020**, *120*, 464.

4. Corma, A.; Garci, H.; *Chem. Soc. Rev.* **2008**, *37*, 2096.

5. Alshammari, A. S.; *Catalysts* **2019**, *9*, 402.

6. Ciriminna, R.; Falletta, E.; Della Pina, C.; Teles, J. H.; Pagliaro, M.; *Angew. Chem., Int. Ed.* **2016**, *55*, 14210.

7. Liu, X. Y.; Wang, A.; Zhang, T.; Mou, C.; *Nano Today* **2013**, *8*, 403.

8. Sankar, M.; He, Q.; Engel, R. V.; Sainna, M. A.; Logsdail, A. J.; Roldan, A.; Willock, D. J.; Agarwal, N.; Kiely, C. J.; Hutchings, G. J.; *Chem. Rev.* **2020**, *120*, 3890.

9. Liu, L.; Corma, A.; *Chem. Rev.* **2018**, *118*, 4981.

10. Du, Y.; Sheng, H.; Astruc, D.; Zhu, M.; *Chem. Rev.* **2020**, *120*, 526.

11. Qian, K.; Kumar, A.; Zhang, H.; Bellmer, D.; Huhnke, R.; *Renewable Sustainable Energy Rev.* **2015**, *42*, 1055.

12. Cha, J. S.; Park, S. H.; Jung, S. C.; Ryu, C.; Jeon, J. K.; Shin, M. C.; Park, Y. K.; *J. Ind. Eng. Chem.* **2016**, *40*, 1.

13. Zhang, X.; Gao, B.; Creamer, A. E.; Cao, C.; Li, Y.; *J. Hazard. Mater.* **2017**, *338*, 102.

14. Lee, J.; Kim, K.; Kwon, E. E.; *Renewable Sustainable Energy Rev.* **2017**, *77*, 70.

15. Lopes, R. P.; Astruc, D.; *Coord. Chem. Rev.* **2021**, *426*, 213585.

16. Jiang, S. F.; Ling, L. L.; Xu, Z.; Liu, W. J.; Jiang, H.; *Ind. Eng. Chem. Res.* **2018**, *57*, 13055.

17. Lara, L. R. S.; Zottis, A. D.; Elias, W. C.; Faggion Jr., D.; de Campos, C. E. M.; Acuña, J. J. S.; Domingos, J. B.; *RSC Adv.* **2015**, *5*, 8289.

18. Aditya, T.; Pal, A.; Pal, T.; *Chem. Commun.* **2015**, *51*, 9410.

19. Zhao, P.; Feng, X.; Huang, D.; Yang, G.; Astruc, D.; *Coord. Chem. Rev.* **2015**, *287*, 114.

20. Hervés, P.; Pérez-Lorenzo, M.; Liz-Marzán, L. M.; Dzubiella, J.; Lub, Y.; Ballauff, M.; *Chem. Soc. Rev.* **2012**, *41*, 5577.

21. Wang, Q.; Astruc, D.; *Chem. Rev.* **2020**, *120*, 1438.

22. Pradhan, N.; Pal, A.; Pal, T.; *Colloids Surf., A* **2002**, *196*, 247.

23. Wunder, S.; Polzer, F.; Lu, Y.; Mei, Y.; Ballauff, M.; *J. Phys. Chem. C* **2010**, *114*, 8814.

24. Hummers Jr., W. S.; Offeman, R. E.; *J. Am. Chem. Soc.* **1958**, *80*, 1339.

25. Wang, L.; Zhang, J.; Wang, A.; *Colloids Surf., A* **2008**, *322*, 47.

26. Zhou, X.; Zeng, Z.; Zeng, G.; Lai, C.; Xiao, R.; Liu, S.; Huang, D.; Qin, L.; Liu, X.; Li, B.; Yi, H.; Fu, Y.; Li, L.; Wang, Z.; *Chem. Eng. J.* **2020**, *383*, 123091.

27. Yan, J.; Yang, L.; Qian, L.; Han, L.; Chen, M.; *Environ. Pollut.* **2020**, *261*, 114020.

28. Fan, Z.; Zhang, Q.; Gao, B.; Li, M.; Liu, C.; Qiu, Y.; *Chemosphere* **2019**, *217*, 85.

29. Gasparov, L. V.; Tanner, D. B.; Romero, H. B. G.; Margaritondo, G.; Forró, L.; *Phys. Rev. B: Condens. Matter Mater. Phys.* **2000**, *62*, 7939.

30. Wang, B.; Li, Y.; Wang, L.; *Chemosphere* **2019**, *237*, 124454.

31. Guimarães, T.; Teixeira, A. P. C.; Oliveira, A. F.; Lopes, R. P.; *New J. Chem.* **2020**, *44*, 3310.

32 Pourhassan, F.; Khalifeh, R.; Eshghi, H.; *Fuel* **2021**, *287*, 119567.

33. Marsh, H.; Yan, D. S.; O'Grady, T. M.; Wennerberg, A.; *Carbon* **1984**, *22*, 603.

34. Jiang, S. F.; Xi, K. F.; Yang, J.; Jiang, H.; *Chemosphere* **2019**, *227*, 63.

35. Karunanayake, A. G.; Todd, O. A.; Crowley, M. L.; Ricchetti, L. B.; Pittman Jr., C. U.; Anderson, R.; Mlsna, T. E.; *Chem. Eng. J.* **2017**, *319*, 75.

36. Liyanage, A. S.; Canaday, S.; Pittman Jr., C. U.; Mlsna, T.; *Chemosphere* **2020**, *258*, 127336.

37. Sahiner, N.; Karakoyun, N.; Alpaslan, D.; Aktas, N.; *Int. J. Polym. Mater.* **2013**, *62*, 590.